Structure of the Mechanosensitive Channel MscS Embedded in the Membrane Bilayer

Tim Rasmussen, Vanessa J. Flegler, Akiko Rasmussen and Bettina Böttcher

Biocenter and Rudolf Virchow Center, *Universität Würzburg, Haus D15, Josef-Schneider-Str. 2, 97080 Würzburg, Germany*

Correspondence to Tim Rasmussen and Bettina Böttcher:. *tim.rasmussen@uni-wuerzburg.de, vanessa.flegler@uni-wuerzburg.de, bettina.boettcher@uni-wuerzburg.de*
https://doi.org/10.1016/j.jmb.2019.07.006
Edited by Nieng Yan

Abstract

Since life has emerged, gradients of osmolytes over the cell membrane cause pressure changes in the cell and require tight regulation to prevent cell rupture. The mechanosensitive channel of small conductance (MscS) releases solutes and water when a hypo-osmotic shock raises the pressure in the cell. It is a member of a large family of MscS-like channels found in bacteria, archaea, fungi and plants and model for mechanosensation. MscS senses the increase of tension in the membrane directly by the force from the lipids, but the molecular mechanism is still elusive. We determined the lipid interactions of MscS by resolving the structure of *Escherichia coli* MscS embedded in membrane discs to 2.9-Å resolution using cryo-electron microscopy. The membrane is attached only to parts of the sensor paddles of MscS, but phospholipid molecules move through grooves into remote pockets on the cytosolic side. On the periplasmic side, a lipid bound by R88 at the pore entrance is separated from the membrane by TM1 helices. The N-terminus interacts with the periplasmic membrane surface. We demonstrate that the unique membrane domain of MscS promotes deep penetration of lipid molecules and shows multimodal interaction with the membrane to fine-tune tension sensing.

Introduction

Crystal structures [1–7] have shown that mechanosensitive channel of small conductance (MscS) is formed by seven identical subunits. Each of the subunits contributes three transmembrane (TM) helices to the channel. The two N-terminal helices (TM1 and TM2) connected by a loop shape a paddle that is tilted away from the channel axis at the cytosolic side. The third helix is kinked at G113, the N-terminal half forms the pore (TM3a), while the C-terminal half (TM3b) joins it with the C-terminal vestibule that assembles a cage-like structure across the channel entrance on the cytosolic side. The different tilt of the paddles and the pore-forming helices gives rise to a large lipid accessible cavity.

MscS can sense dangerously high pressures in the cell via the increased tension in the membrane, but the sensing mechanism is still not well understood [8]. However, it is agreed that the force-from-lipid underlies tension sensing [9,10]. The mechanism of tension sensing has been controversially discussed because high-resolution structural data were derived from crystal structures of MscS in the detergent micelle [1–7] devoid of the lipidic environment. Therefore, the interplay of lipids with the protein scaffold remained elusive, and doubts have been raised on the relevance of these crystal structures [11–16]. In particular, the tilt of the paddles that gives rise to an overall cone-shaped membrane domain has been questioned. In addition, the crystal structures cannot provide information where exactly the membrane attaches to the protein complex. To resolve this controversy on detergent solubilized channels, we determined the structure of *Escherichia coli* MscS embedded in membrane discs, known as nanodiscs [17], providing a solid basis for the evaluation of protein–lipid interactions in MscS, which will allow us to better understand the tension sensing mechanism of MscS.

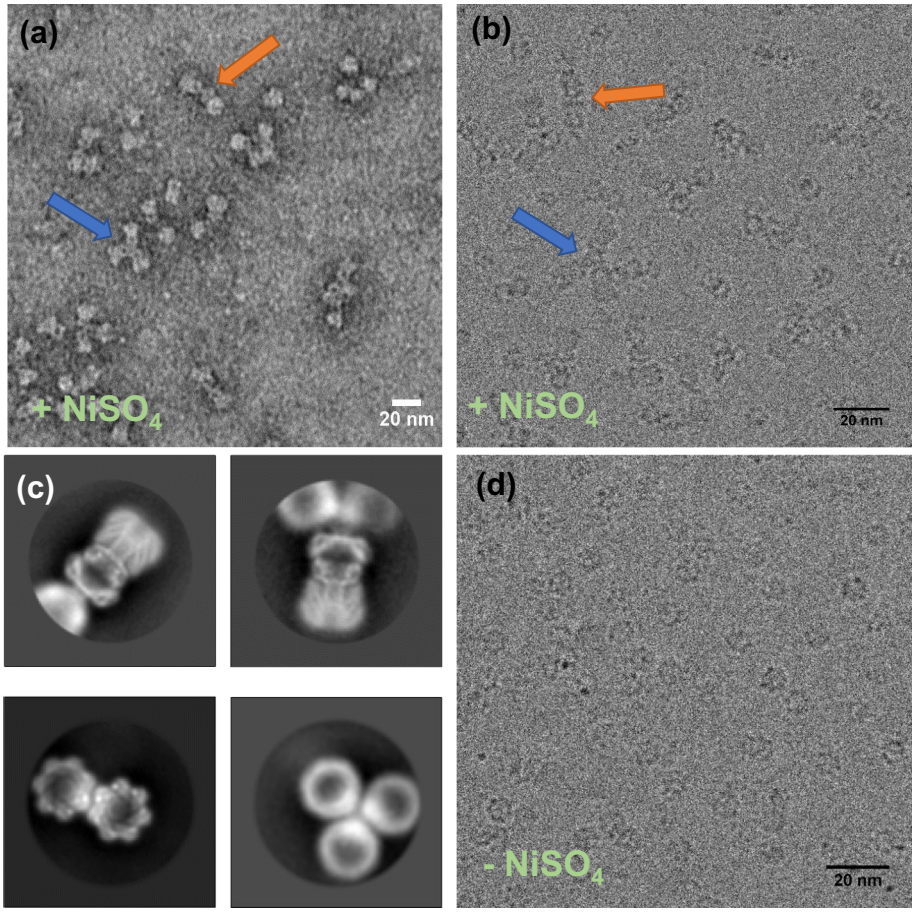

Fig. 1. Oligomerization of MscS complexes. (a) Negatively stained micrograph of 0.05 mg/ml MscS in nanodiscs in the presence of 0.2 mM $NiSO_4$. The stain is penetrating the vestibules, which are clearly visible. A trimer of MscS complexes is marked by a blue arrow and a dimer with an orange arrow. (b) Cryo-EM micrograph of a similar sample than in panel a but with a higher MscS concentration of 0.4 mg/ml. (c) 2D classes of MscS complex oligomers. The top row shows 2D classes where MscS forms oligomers over the β-barrel triggered by adding 0.2 mM $NiSO_4$. Particles of these classes were not used for the reconstruction, but classes shown in Fig. 2b. In the bottom row, a different kind of oligomerization is shown where the complexes lie side-by-side. Its occurrence is independent of the presence of $NiSO_4$. The edges of the boxes correspond to 26.6 nm. (d) Cryo-EM micrograph of a MscS sample without $NiSO_4$ where the particles are predominantly orientated along the 7-fold axis.

Results and Discussion

Particles of MscS are preferentially oriented with most projections along the 7-fold symmetry axis. Initial 2D classifications show only 1%–2% of particles in projections perpendicular to the symmetry axis (Fig. 1d). Therefore, we induced a controlled oligomerization of particles via the C-terminal His_6-tag at the end of the β-barrel by addition of 0.2 mM $NiSO_4$ 5 min before freezing (Fig. 1a and b). This allows particles to interact with each other over the His_6-tags presumably by Ni-coordination. Oligomerization changes the preference in orientations with about 10 times more side views in 2D classifications as without addition of $NiSO_4$. Projections along the 7-fold symmetry axis (Fig. 2b, first row) were excluded from further processing (Fig. 2d) as their overrepresentation leads to distorted maps. The final map has a resolution of 2.9 Å (Figs. 2c, S1 and S2).

The overall structure of MscS shows two clear domains: the vestibule domain and the helical paddle domain, both are separated by TM3b (Fig. 3). The nanodisc is located at the periplasmic half of the helical paddle domain, suggesting that the helical domain is only partly embedded in the membrane. This is in agreement with fluorescence quenching experiments of a series of tryptophan mutants along TM1 by brominated lipids [18]. Especially TM3b, the cytosolic part of the cavity underneath TM3b and the hairpin of the paddle project out of the general membrane level. At the periplasmic side, TM1 starts at residue Q21 some 20 Å above the loop that connects TM3a and TM2. This staggered arrangement relative to the

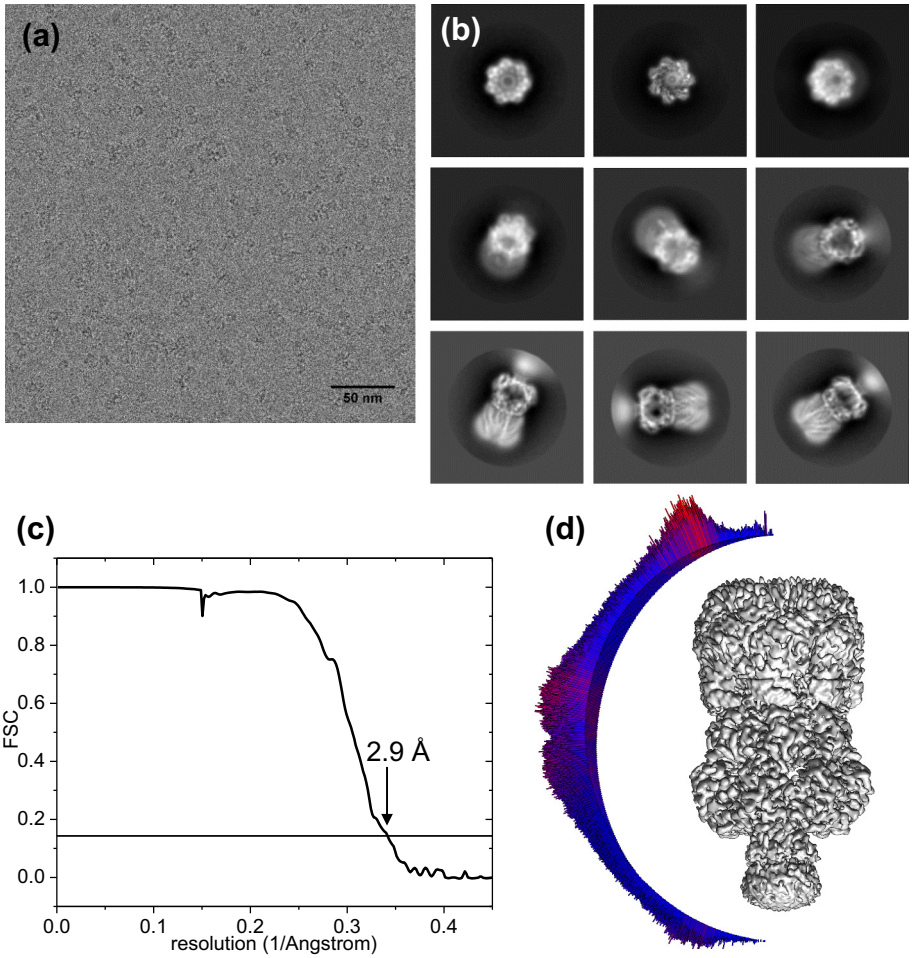

Fig. 2. EM of MscS and reconstruction. (a) Typical micrograph of MscS in nanodiscs with 0.2 mM $NiSO_4$. (b) Typical 2D classes. The edge of the boxes corresponds to 26.6 nm. Classes along the 7-fold axis, like the first two classes, were not used for the reconstruction but indicate the overall symmetry of the complex. (c) FSC curve according to the "gold standard" generated with *Relion*. The horizontal line represents a value of 0.143. (d) Angular distribution of the final refinement.

membrane level suggests that TM2 and TM3a are partly embedded into the cytosolic leaflet of the membrane and only TM1 extends to the periplasmatic side of the membrane.

We find that the structure of MscS in the membrane resembles the earlier crystal structures of the closed conformation solubilized in foscoline micelles (Fig. S3) [1,2]. For a membrane-embedded MscS, the closed conformation is expected, while MscS solubilized in dodecyl maltoside (DDM) [4,6,7] or having the mutation A106V [3] adopted an open conformation in crystals. Most differences in comparison to the first closed structure are due to deviations of the crystal structure from C7 symmetry, while we find no indication for deviation from the C7 symmetry in our data (Fig. 2b).

Beside the protein structure, additional density is observed within the complex. Tubular densities of the fatty acid chains and branching points allowed us to model three phospholipid molecules per subunit (Fig. 4). Two of them lie parallel to TM3b at the cytosolic end of the pockets, and one of them seems to form a salt bridge with R59. Interestingly, the mutation R59L causes a strong gain-of-function phenotype [18]. Less well-resolved density indicates that lipids continuously fill the gaps between the paddles from the membrane level up to the lipids close to TM3b (Fig. 3a). Molecular dynamics simulation confirms the positioning of lipids in our structure [7,19].

We find the best-resolved lipid at a different location away from TM3b toward the periplasmic side. The head group of this lipid forms a salt bridge with R88 at the loop between TM2 and TM3a (Fig. S4). Its orientation with the fatty acid chains facing parallel to the paddles toward the cytosol suggests that it originated from the

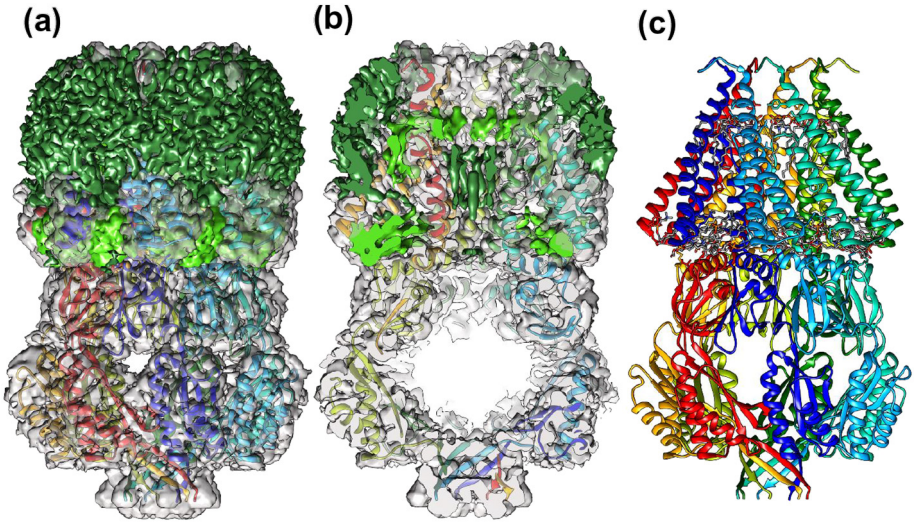

Fig. 3. Structure of MscS in nanodiscs. The cytosolic vestibule domain is shown at the bottom, while the helical domain toward the periplasm at the top. (a) The EM map together with the model shows the nanodisc at the top (dark green). Three phospholipid molecules per subunit were resolved and modeled (light green). (b) A cut through the structure shows a lipid between paddle and TM3a and elongated densities in the central pore. (c) Model of MscS with different colors for the subunits. Disordered density below the C-terminal β-barrel is omitted in this figure (but see Figs. 2 and 4).

periplasmatic leaflet of the membrane. Although the hydrophobic tails are exposed to the membrane core, the head group seems to have no direct access to the membrane interface because the N-terminal ends of TM1 block the way (Fig. 5b). Comparison with the open crystal structures

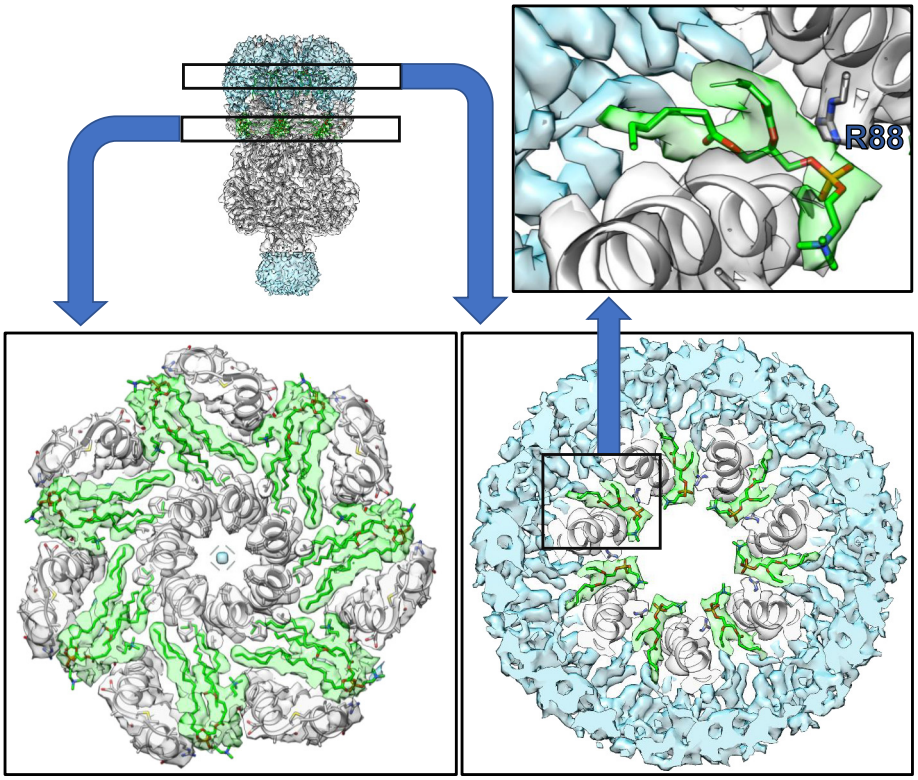

Fig. 4. Phospholipid molecules bound to MscS. Close to TM3b toward the periplasm, two lipids per subunit are resolved (left). At the periplasmic end of the central pore, another lipid molecule is resolved with the head group coordinated by R88 facing into the pore (right). Densities of the lipids (green), the protein (gray) and unmodeled density, mainly from the nanodisc (blue), are shown.

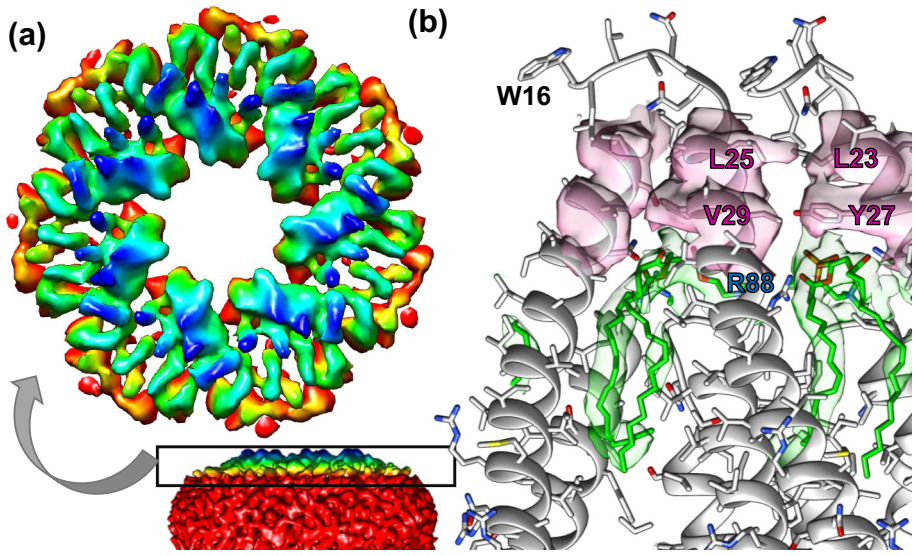

Fig. 5. N-terminal region of MscS. (a) The N-terminal region preceding TM1 spreads on the periplasmic membrane surface (colored by location along the C7 axis). (b) N-terminal residues of TM1 (density in surrounding colored pink) block the way for the bound lipid (green) toward the membrane interface. This lipid is coordinated by R88 (blue).

suggests that this lipid only can equilibrate with the membrane in the open conformation because under these conditions, the TM1s move apart at their N-termini and provide a route for the trapped lipid to connect with the periplasmic leaflet (Fig. 6). Since the loop between TM2 and TM3a, where the lipid is attached, is located in the middle of the membrane, the lipid has not only to move outward but also on the membrane normal toward the periplasm to equilibrate with the membrane. The open crystal structures support such movement because the more tilted paddle within the

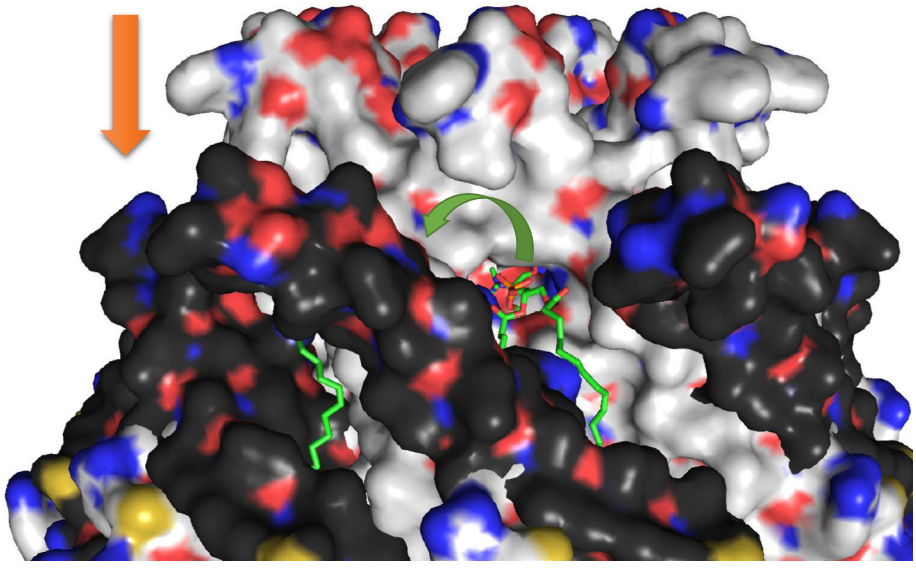

Fig. 6. Comparison of the EM structure in membranes with the open crystal structure in micelles (PDB: 5AJI). The closed EM structure is shown in light gray and the open crystal structure in dark gray surface representation. A modeled lipid molecule (green) in the EM structure is coordinated by R88, and its head group is separated from the periplasmic head group region by the side chains of the N-terminal TM1. When the channel is opening, the N-terminal end of TM1 moves approximately 25 Å outward and toward the cytosol (orange arrow). This move opens a gap between TM1 helices on the periplasmic side and also brings R88 closer to the N-terminal end of TM1 and with this to the head group region of the periplasmic leaflet. Thus, the comparison suggests that the lipid cannot equilibrate with the membrane in the closed state but in the open state (schematically shown by the green arrow).

membrane brings the TM2–TM3a loop closer to the periplasmic interface of the membrane (Fig. 6). It has been shown that an R88W mutation, in which the salt bridge with the lipid head group would be disrupted, requires higher pressures to open the channel [20]. An R88S mutation also shows a loss-of-function phenotype in electrophysiological experiments [21]. Elongated densities can also be seen within the pore (Fig. 3b). Since they are not located on the central symmetry axis, they could represent real density and not only noise, which is expected to accumulate on the axis. It is possible that these densities are caused by lipid molecules blocking the central pore from the periplasmic side. This interpretation is supported by fluorescence quenching experiments of the mutants A94W and G101W, which show a strong quenching with brominated lipids [18].

The structure of the N-terminus beyond TM1 has not been resolved in any structure. Our structure shows that TM1 is longer than previously observed and forms a shielded periplasmatic anti-chamber in front of the narrow pore formed by TM3 (Fig. S5a). Upstream of TM1 the N-terminus lies on the periplasmatic interface of the membrane projecting radially outward (Fig. 5a). Our model starts from residue 16 onward, but the pattern in the density map suggests that the N-terminus spreads further as flexible tentacles on the periplasmic membrane surface. The structure suggests that the interaction with the lipids stabilizes the tentacles and explains why they are not resolved in the earlier crystal structures, which were devoid of a membrane. The lower resolution of the tentacle in comparison with the rest of the channel indicates more flexibility, which is in agreement with earlier electron paramagnetic resonance data [11]. W16 is located close to the hinge between TM1 and the N-terminal tentacles and is exposed to the membrane. It is the only tryptophan in the membrane domain of MscS; none is found at the cytosolic interface. The amphipathic character of tryptophan explains its anchoring function in membrane proteins and the positioning of W16 at the hinge suggests that it provides a key interaction with the membrane at the periplasmic surface. We showed earlier that mutation of this residue impacts on the gating of MscS [22]. Electrophysiological experiments showed that even a conservative mutation to tyrosine makes it harder to open the channel. A mutation to leucine with no amphiphilicity is even harder to open demonstrating the sensitivity of this hinge. MscS with deletion of residue 8–12 or even 8–21 was still able to protect in osmotic downshock assays, indicating that MscS retained at least partial functionality [23]. However, this functional assay is not suitable to indicate subtle changes.

The presented cryo-electron microscopy (cryo-EM) structure refines our understanding how MscS interacts with the membrane in different ways: The membrane attaches only on the periplasmic side of the paddles. The cryo-EM structure resolves lipid molecules in the pockets of MscS. It has been suggested that lipid extrusion from the pockets at higher-membrane tension triggers activation [7]. Data on R59 support this model: R59 forms a salt bridge with a lipid in the pocket. If this salt bridge is lost as in the mutant R59L, the lipid can be more easily extracted from the pocket resulting in a strong gain-of-function phenotype [18]. Our structure shows that parts of the pockets lie beyond the membrane on the cytosolic side and lipids slide within the grooves between the paddles into the pockets. Only these grooves provide an energetically favorable hydrophobic environment to reach the remote pockets at TM3b (Fig. S5b). On the periplasmic side, the TM1 helices come close together so that a lipid resolved at the loop between TM2 and TM3a seems not be able to pass with its head group to the head group region of the periplasmic membrane leaflet. Thus, removal of this lipid cannot be the cause for tension sensing because the sensing model would require the extrusion to preside the conformational change. Interaction of this lipid with MscS seems to be still important because disruption of this interaction by the mutation R88W or R88S causes loss-of-function and instability of the complex [20,21].

The overall conical shape of the membrane domain was the basis for an alternative tension-sensing mode of MscS [24]. While we can confirm the conical shape of the complex in a membranous environment, we cannot see directly a local membrane curvature in the nanodiscs with a diameter of about 17 nm [17]. To answer this question, a wider membrane embedment would be necessary. The cryo-EM structure revealed another mode of interaction with the membrane. At low resolution, we could resolve the N-terminal domain of MscS forming tentacles on the outer-membrane surface. This interaction could play a role in tension sensing, and it has been suggested that amphipathic helices could be at the basis of tension sensing in general [25,26].

Our EM structure emphasizes that the most dramatic conformational changes between open [7] and closed channel happen at the N-terminal end of TM1 (about 25-Å movement). This suggests a relative movement of the periplasmic head group region of the membrane toward the C-terminal MscS complex beyond the paddle, which could compensate a membrane thinning expected for high tensions [27,28] (Fig. 6). In addition, the parting ends of TM1 helices open the complex up for equilibration with membrane lipids.

Crystal structures and this EM structure can be classed into two conformational states of MscS, which have been suggested to be open and closed

states. However, electrophysiology showed that MscS can have two more adapted states, states with no activity despite tension on the membrane [29–31]. It has been suggested that either the conformation of TM3 [14] or lipids blocking the pore could be the molecular basis of adaptation [8,32,33]. Some support for the latter adaptation model is provided by our EM structure because we find a lipid at the edge of the pore at the loop between TM2 and TM3a, which might get access to the pore. In addition, we see elongated densities in the pore, which could be lipids. Residues within the pore, A94W and G101W, are lipid accessible as indicated by fluorescence quenching [18]. Interestingly, the mutations G101D [21] and A98S [34] show less adaptation, which could be caused by the decreased hydrophobicity in the mutant pore and consequently less lipid blockage. On the other hand, other adaptation mutations distant from TM3a have been described (see, e.g., Refs. [14,18]) that are not obviously related to this adaptation model. Perhaps more than one adaptation mechanism exists in MscS, which is also expected from electrophysiology studies [14].

Our structure reveals different modes of interactions of MscS with the membrane and their lipids and consequently is in agreement with different alternative tension-sensing models. Detailed molecular simulations and mutagenesis studies will be required to dissect the relative energetic contribution of these models to tension sensing.

Materials and Methods

Materials

Chemicals were obtained from Sigma-Aldrich if not specified otherwise.

Expression and purification of MscS

MscS was expressed and purified as described before [20,22,35] with some modifications described here. MscS was expressed from a pTrc vector with C-terminal His_6-tag in the *E. coli* strain MJF641, which has all genes for mechanosensitive channels deleted [36]. MscS was expressed in Luria-Bertani medium by induction with 0.8 mM IPTG for 4 h at 30 °C. Cells were harvested by centrifugation at 5000 *g* for 30 min and stored at − 80 °C until further use. Cells were suspended in 5 ml/g cells phosphate-buffered saline, and 1 mM phenylmethane sulfonyl fluoride was added. Cells were lysed by addition of 5 mM EDTA and 10 mg/g cells lysozyme and a freeze–thaw cycle with liquid nitrogen. Cell debris were centrifuged at 7000 *g* for 30 min and suspended with a Teflon-in-glass homogenizer in a buffer containing 1% dodecyl-β-maltoside (DDM; from Glycon, Germany), 50 mM sodium phosphate buffer (pH 7.5), 300 mM NaCl, 10% (w/v) glycerol, 10 mM $MgCl_2$, 0.01% DNase (Roche) and 50 mM imidazole. After a 1-h incubation on ice, the suspension was centrifuged at 7000*g* for 30 min and filtered through 0.2-μm syringe filters (Roth, Germany). For a typical preparation from 4 to 5 g cells, solubilized MscS is bound to 0.5 g Ni-NTA agarose resin loaded into 10-ml plastic columns. The resin is then washed with 30 ml of washing buffer containing 0.05% DDM, 50 mM sodium phosphate buffer (pH 7.5), 300 mM NaCl, 10% (w/v) glycerol and 50 mM imidazole. MscS was then eluted with washing buffer containing 300 mM imidazole. The peak fraction was further purified by size exclusion chromatography on a 25-ml Superose 6 column (GE Healthcare) using the HPLC buffer containing 50 mM Hepes (pH 7.5), 150 mM NaCl and 0.03% DDM.

Reconstitution of MscS into nanodiscs

pMSP1E3D1 was a gift from Stephen Sligar (Addgene plasmid no. 20066; http://n2t.net/addgene:20066; RRID:Addgene_20066) and was purified as described earlier [17]. A solution of the membrane scaffold protein MSP1E3D1 [17] without His_6-tag was prepared in reconstitution buffer of 20 mM Hepes (pH 7.5), 100 mM NaCl, 10% glycerol and 50 mM sodium cholate (Roth, Germany). A lipid film was made in a glass tube by solving 100 mM asolectin from soybean in chloroform and then removing the chloroform in a nitrogen gas stream. Phosphatidylcholine, the main component of asolectin, is not native to *E. coli* but closely related to phosphatidyethanolamine, the main component of *E. coli* membranes. Many functional studies on reconstituted MscS showed no difference between phosphatidylcholine and phosphatidylethanolamine [37,38]. Direct detection of protein–lipid interactions at several locations in MscS by fluorescence showed also no difference [7]. The lipids were solved in reconstitution buffer without glycerol but with 200 mM sodium cholate by removing air with argon, warming the tube for 1 min in warm water, and 10 min sonification in an ultrasonic bath. Six hundred sixteen microliters of 10 μM MscS was mixed with 144 μl of 348 μM MSP1E3D1 and 40 μl of 100 mM phospholipids and incubated on ice for 2.5 h. Afterward, 500 mg of wet Biobeads SM2 was added, and the reaction tube was rotated in the cold room at 4 °C overnight. MscS reconstituted in nanodiscs is bound to 0.25 g Ni-NTA agarose resin loaded into a 10-ml plastic column while nanodiscs containing no MscS flow through the column. MscS integrated in nanodiscs was then eluted using a buffer containing 20 mM Hepes (pH 7.5), 100 mM NaCl and 300 mM imidazole. The sample was then

Table 1. Unified map parameters, model building and validation

Map parameters	
Final particles (no.)	302,157
Symmetry imposed	C7
Map resolution (Å)	2.9
FSC threshold	0.143
Map resolution range (Relion local res.) (Å)	2.78–4.90
Map sharpening *B* factor (Å^2)	−139
Model refinement	
Initial model used (PDB code)	2OAU
Model composition	
Non-hydrogen atoms	15,309
Protein residues	1855
Ligands	21
B factors (Å^2)	
Protein	88
Ligand	120
Validation	
MolProbity score	1.64
Clashscore	5.82
Poor rotamers (%)	0.47
R.m.s. deviations	
Bond lengths (Å)	0.008
Bond angles (°)	1.164
Ramachandran plot	
Favored (%)	95.44
Allowed (%)	4.56
Outliers (%)	0.00

further purified by size exclusion chromatography using a 25-ml Superose 6 column and a buffer containing 50 mM Hepes (pH 7.5) and 50 mM NaCl. Peak fractions were pooled and concentrated with an Amicon 100 K Ultra-0.5 centrifugal filter device (Millipore) at 12,000*g* at 4 °C to a concentration of 0.4 mg/ml.

Cryo-EM

Samples of MscS embedded in nanodiscs were incubated for 5 min with 0.2 mM $NiSO_4$ (Fig. 1) and then frozen on R1.2/1.3 holey carbon-coated copper 400 grids (Quantifoil) employing a Vitrobot IV (FEI) freezing device. The settings for the Vitrobot were as follows: 3-s blotting time, 0 blot force, 45-s waiting time, 0-s drain time and 1 blot in total with a humidity of 100% and temperature of 4 °C. Data were acquired on a FEI Titan Krios G3 microscope with a direct Falcon III detector at a magnification of 75,000 and a defocus range from 0.9 to 2.4 µm. This corresponds to a calibrated pixel size of 1.0635 Å. Samples of this study served as test for the newly established Krios microscope at the cryoEM facility in Würzburg so that several data sets at different conditions were collected (Table S1). It turned out that the best map could be obtained by unifying data from all data sets at a late state of data analysis (see below) despite the fact that different conditions were used for these measurements. The feasibility of this approach was confirmed by the fact that data from different measuring conditions were not separated in 3D classifications.

Data analysis

Movies were motion corrected and dose weighted with the program *MotionCor2* [39] and then further processed in *Relion* 2.1 and 3.0 beta [40]. The contrast transfer functions were determined with the program *CTFFind4* [41]. Particles were first auto-picked with a gaussian blob as reference and after 2D classification with appropriate class averages [42]. Particles were cleaned up by two rounds of 2D classification, and predominately side views and diagonal views were selected while top views along the C7 symmetry axis were rejected for further image processing. As an initial model, a map of YnaI was used (EMDB: 3035) [43]. After refinement, a 3D classification was executed, and the best class was used for another refinement. Data were reextracted with a large box size of 600 × 600 and a per-particle CTF correction and beam tilt correction was performed in *Relion* with the *CTFrefine* routine for each data set. Only after this step, data from different data sets were unified and another round of *Autorefine* was executed. The resolution is given after gold standard refinement as implemented in *Relion* [44]. The local resolution was estimated with the local resolution tool of *Relion*. A molecular model was obtained with the program *Coot* version 0.8.9.1 [45] with the closed crystal structure as a starting model (PDB: 2OAU). The model was further refined within *Phenix* realspace.refine version 1.13-2998 [46] and validated with *MolProbity.* Images of the densities and models were obtained with the programs *Chimera* 1.11 [47] and *PyMOL* version 1.8. Details of the data analysis are summarized in Table 1.

Accession numbers

The filtered map and unfiltered half maps are available in the electron microscopy database (EMDB) under the accession number EMDB ID: 4919 and the model in the PDB database under the code PDB ID: 6RLD.

Acknowledgments

We thank Julian Lenhart and Christian Kraft for technical assistance. We thank Stephen Sligar for the provision of plasmid pMSP1E3D1. This work was supported by the Deutsche Forschungsgemeinschaft (DFG project grant Bo1150/15-1 and DFG equipment grant INST 93/903-1 FUGG).

Author Contributions

T.R., V.F. and A.R. acquired data. All authors analyzed the data, and wrote and edited the manuscript. T.R. and B.B. concepted and supervised the study. B.B. obtained funding.

Declaration of Competing Interest

The authors declare no competing interests.

Appendix A. Supplementary data

Supplementary data to this article can be found online at https://doi.org/10.1016/j.jmb.2019.07.006.

Received 3 May 2019;
Received in revised form 12 June 2019;
Accepted 1 July 2019
Available online 7 July 2019

Keywords:
bacterial channel;
cryo-electron microscopy;
force-from-lipid principle;
lipid–protein interaction;
nanodiscs

Abbreviations:
cryo-EM, cryo-electron microscopy; DDM, dodecyl-β-maltoside; MscS, mechanosensitive channel of small conductance; TM, transmembrane.

References

[1] R.B. Bass, P. Strop, M. Barclay, D.C. Rees, Crystal structure of *Escherichia coli* MscS, a voltage-modulated and mechanosensitive channel, Science (80-.) 298 (2002) 1582–1587, https://doi.org/10.1126/science.1077945.

[2] S. Steinbacher, R. Bass, P. Strop, D.C. Rees, Mechanosensitive Ion Channels, Part A, Elsevier, 2007https://doi.org/10.1016/S1063-5823(06)58001-9.

[3] W. Wang, S.S. Black, M.D. Edwards, S. Miller, E.L. Morrison, W. Bartlett, C. Dong, J.H. Naismith, I.R. Booth, The structure of an open form of an *E. coli* mechanosensitive channel at 3.45 Å resolution, Science (80-.) 321 (2008) 1179–1183, https://doi.org/10.1126/science.1159262.

[4] C. Pliotas, R. Ward, E. Branigan, A. Rasmussen, G. Hagelueken, H. Huang, S.S. Black, I.R. Booth, O. Schiemann, J.H. Naismith, Conformational state of the MscS mechanosensitive channel in solution revealed by pulsed electron-electron double resonance (PELDOR) spectroscopy, Proc. Natl. Acad. Sci. U. S. A. 109 (2012) E2675–E2682, https://doi.org/10.1073/pnas.1202286109.

[5] X. Zhang, J. Wang, Y. Feng, J. Ge, W. Li, W. Sun, I. Iscla, J. Yu, P. Blount, Y. Li, M. Yang, Structure and molecular mechanism of an anion-selective mechanosensitive channel of small conductance, Proc. Natl. Acad. Sci. U. S. A. 109 (2012) 18180–18185, https://doi.org/10.1073/pnas.1207977109.

[6] J. Lai, Y. Poon, J. Kaiser, D. Rees, Open and shut: crystal structures of the dodecylmaltoside solubilized mechanosensitive channel of small conductance from *Escherichia coli* and Helicobacter at 4.4 Å and 4.1 Å resolutions, Protein Sci. 22 (2013) 502–509.

[7] C. Pliotas, A.C.E. Dahl, T. Rasmussen, K.R. Mahendran, T.K. Smith, P. Marius, J. Gault, T. Banda, A. Rasmussen, S. Miller, C.V. Robinson, H. Bayley, M.S.P. Sansom, I.R. Booth, J.H. Naismith, The role of lipids in mechanosensation, Nat. Struct. Mol. Biol. 22 (2015) 991–998, https://doi.org/10.1038/nsmb.3120.

[8] T. Rasmussen, How do mechanosensitive channels sense membrane tension? Biochem. Soc. Trans. 44 (2016) 1019–1025, https://doi.org/10.1042/BST20160018.

[9] A. Anishkin, S.H. Loukin, J. Teng, C. Kung, Feeling the hidden mechanical forces in lipid bilayer is an original sense, Proc. Natl. Acad. Sci. U. S. A. 111 (2014) 7898–7905, https://doi.org/10.1073/pnas.1313364111.

[10] J. Teng, S. Loukin, A. Anishkin, C. Kung, The force-from-lipid (FFL) principle of mechanosensitivity, at large and in elements, Pflügers Arch. Eur. J. Physiol. 467 (2015) 27–37, https://doi.org/10.1007/s00424-014-1530-2.

[11] V. Vásquez, M. Sotomayor, D.M. Cortes, B. Roux, K. Schulten, E. Perozo, Three-dimensional architecture of membrane-embedded MscS in the closed conformation, J. Mol. Biol. 378 (2008) 55–70, https://doi.org/10.1016/j.jmb.2007.10.086.

[12] C. Kung, B. Martinac, S. Sukharev, Mechanosensitive channels in microbes, Annu. Rev. Microbiol. 64 (2010) 313–329, https://doi.org/10.1146/annurev.micro.112408.134106.

[13] V. Belyy, A. Anishkin, K. Kamaraju, N. Liu, S. Sukharev, The tension-transmitting 'clutch' in the mechanosensitive channel MscS, Nat. Struc. Mol. Biol. 17 (2010) 451–458.

[14] B. Akitake, A. Anishkin, N. Liu, S. Sukharev, Straightening and sequential buckling of the pore-lining helices define the gating cycle of MscS, Nat. Struct. Mol. Biol. 14 (2007) 1141–1149, https://doi.org/10.1038/nsmb1341.

[15] A. Anishkin, B. Akitake, S. Sukharev, Characterization of the resting MscS: modeling and analysis of the closed bacterial mechanosensitive channel of small conductance, Biophys. J. 94 (2008) 1252–1266, https://doi.org/10.1529/biophysj.107.110171.

[16] A. Anishkin, S. Sukharev, State-stabilizing interactions in bacterial mechanosensitive channel gating and adaptation, J. Biol. Chem. 284 (2009) 19153–19157, https://doi.org/10.1074/jbc.R109.009357.

[17] I.G. Denisov, B.J. Baas, Y.V. Grinkova, S.G. Sligar, Cooperativity in cytochrome P450 3A4: linkages in substrate binding, spin state, uncoupling, and product formation, J. Biol. Chem. 282 (2007) 7066–7076, https://doi.org/10.1074/jbc.M609589200.

[18] T. Rasmussen, A. Rasmussen, L. Yang, C. Kaul, S. Black, H. Galbiati, S.J. Conway, S. Miller, P. Blount, I.R. Booth, Interaction of the mechanosensitive channel, mscs, with the membrane bilayer through lipid intercalation into grooves and pockets, J. Mol. Biol. (2019)https://doi.org/10.1016/j.jmb.2019.05.043.

[19] P.J. Stansfeld, J.E. Goose, M. Caffrey, E.P. Carpenter, J.L. Parker, S. Newstead, M.S.P. Sansom, MemProtMD: automated insertion of membrane protein structures into explicit lipid membranes, Structure. 23 (2015) 1350–1361, https://doi.org/10.1016/J.STR.2015.05.006.

[20] T. Rasmussen, A. Rasmussen, S. Singh, H. Galbiati, M.D. Edwards, S. Miller, I.R. Booth, Properties of the mechanosensitive channel MscS pore revealed by tryptophan scanning mutagenesis, Biochemistry. 54 (2015) 4519–4530, https://doi.org/10.1021/acs.biochem.5b00294.

[21] M.D. Edwards, W. Bartlett, I.R. Booth, Pore mutations of the *Escherichia coli* MscS channel affect desensitization but not ionic preference, Biophys. J. 94 (2008) 3003–3013, https://doi.org/10.1529/biophysj.107.123448.
[22] A. Rasmussen, T. Rasmussen, M.D. Edwards, D. Schauer, U. Schumann, S. Miller, I.R. Booth, The role of tryptophan residues in the function and stability of the mechanosensitive channel MscS from *Escherichia coli*, Biochemistry. 46 (2007) 10899–10908, https://doi.org/10.1021/bi701056k.
[23] S. Miller, W. Bartlett, S. Chandrasekaran, S. Simpson, M. Edwards, I.R. Booth, Domain organization of the MscS mechanosensitive channel of *Escherichia coli*, EMBO J. 22 (2003) 36–46, https://doi.org/10.1093/emboj/cdg011.
[24] R. Phillips, T. Ursell, P. Wiggins, P. Sens, Emerging roles for lipids in shaping membrane-protein function, Nature. 459 (2009) 379–385, https://doi.org/10.1038/nature08147.
[25] I. Iscla, R. Wray, P. Blount, On the structure of the N-terminal domain of the MscL channel: helical bundle or membrane interface, Biophys. J. 95 (2008) 2283–2291, https://doi.org/10.1529/biophysj.107.127423.
[26] N. Bavi, D.M. Cortes, C.D. Cox, P.R. Rohde, W. Liu, J.W. Deitmer, O. Bavi, P. Strop, A.P. Hill, D. Rees, B. Corry, E. Perozo, B. Martinac, The role of MscL amphipathic N terminus indicates a blueprint for bilayer-mediated gating of mechanosensitive channels, Nat. Commun. 7 (2016) 11984, https://doi.org/10.1038/ncomms11984.
[27] M. Goulian, O.N. Mesquita, D.K. Fygenson, C. Nielsen, O.S. Andersen, A. Libchaber, Gramicidin channel kinetics under tension, Biophys. J. 74 (1998) 328–337, https://doi.org/10.1016/S0006-3495(98)77790-2.
[28] J. Neder, B. West, P. Nielaba, F. Schmid, Coarse-grained simulations of membranes under tension, J. Chem. Phys. 132 (2010) 115101, https://doi.org/10.1063/1.3352583.
[29] S.I. Sukharev, P. Blount, B. Martinac, C. Kung, Mechanosensitive channels of *Escherichia coli*: the MscL gene, protein, and activities, Annu. Rev. Physiol. 59 (1997) 633–657, https://doi.org/10.1146/annurev.physiol.59.1.633.
[30] P. Koprowski, A. Kubalski, Voltage-independent adaptation of mechanosensitive channels in *Escherichia coli* protoplasts, J. Membr. Biol. 164 (1998) 253–262, https://doi.org/10.1007/s002329900410.
[31] N. Levina, S. Tötemeyer, N.R. Stokes, P. Louis, M.A. Jones, I.R. Booth, Protection of *Escherichia coli* cells against extreme turgor by activation of MscS and MscL mechanosensitive channels: identification of genes required for MscS activity, EMBO J. 18 (1999) 1730–1737, https://doi.org/10.1093/emboj/18.7.1730.
[32] X.C. Zhang, Z. Liu, J. Li, From membrane tension to channel gating: a principal energy transfer mechanism for mechanosensitive channels, Protein Sci. (2016)https://doi.org/10.1002/pro.3017.
[33] T. Rasmussen, A. Rasmussen, Bacterial Mechanosensitive Channels, in: J.R. Harrris, E.J. Boekema (Eds.), *Subcellular Biochemistry* 87, Membrane Protein Complexes: Structure and Function, Springer, Singapore 2018, pp. 83–116, https://doi.org/10.1007/978-981-10-7757-9_4.
[34] K. Kamaraju, V. Belyy, I. Rowe, A. Anishkin, S. Sukharev, The pathway and spatial scale for MscS inactivation, J. Gen. Physiol. 138 (2011) 49–57, https://doi.org/10.1085/jgp.201110606.
[35] T. Rasmussen, M.D. Edwards, S.S. Black, A. Rasmussen, S. Miller, I.R. Booth, Tryptophan in the pore of the mechanosensitive channel MscS: assessment of pore conformations by fluorescence spectroscopy, J. Biol. Chem. 285 (2010) 5377–5384, https://doi.org/10.1074/jbc.M109.071472.
[36] M.D. Edwards, S. Black, T. Rasmussen, A. Rasmussen, N.R. Stokes, T.-L. Stephen, S. Miller, I.R. Booth, Characterization of three novel mechanosensitive channel activities in *Escherichia coli*, Channels 6 (2012) 272–281, https://doi.org/10.4161/chan.20998.
[37] S. Sukharev, Purification of the small mechanosensitive channel of *Escherichia coli* (MscS): the subunit structure, conduction, and gating characteristics in liposomes, Biophys. J. 83 (2002) 290–298, https://doi.org/10.1016/S0006-3495(02)75169-2.
[38] T. Nomura, C.G. Cranfield, E. Deplazes, D.M. Owen, A. Macmillan, A.R. Battle, M. Constantine, M. Sokabe, B. Martinac, Differential effects of lipids and lyso-lipids on the mechanosensitivity of the mechanosensitive channels MscL and MscS, Proc. Natl. Acad. Sci. U. S. A. 109 (2012) 8770–8775, https://doi.org/10.1073/pnas.1200051109.
[39] S.Q. Zheng, E. Palovcak, J.P. Armache, K.A. Verba, Y. Cheng, D.A. Agard, MotionCor2: anisotropic correction of beam-induced motion for improved cryo-electron microscopy, Nat. Methods 14 (2017) 331–332, https://doi.org/10.1038/nmeth.4193.
[40] S.H.W.W. Scheres, RELION: implementation of a Bayesian approach to cryo-EM structure determination, J. Struct. Biol. 180 (2012) 519–530, https://doi.org/10.1016/j.jsb.2012.09.006.
[41] A. Rohou, N. Grigorieff, CTFFIND4: fast and accurate defocus estimation from electron micrographs, J. Struct. Biol. 192 (2015) 216–221, https://doi.org/10.1016/j.jsb.2015.08.008.
[42] S.H.W. Scheres, Semi-automated selection of cryo-EM particles in RELION-1.3, J. Struct. Biol. 189 (2015) 114–122, https://doi.org/10.1016/j.jsb.2014.11.010.
[43] B. Böttcher, V. Prazak, A. Rasmussen, S.S. Black, T. Rasmussen, The structure of YnaI implies structural and mechanistic conservation in the MscS family of mechanosensitive channels, Structure 23 (2015) 1705–1714, https://doi.org/10.1016/j.str.2015.06.023.
[44] S.H.W. Scheres, S. Chen, Prevention of overfitting in cryo-EM structure determination, Nat. Methods 9 (2012) 853–854, https://doi.org/10.1038/nmeth.2115.
[45] P. Emsley, B. Lohkamp, W.G. Scott, K. Cowtan, Features and development of coot, Acta Crystallogr. Sect. D Biol. Crystallogr. 66 (2010) 486–501, https://doi.org/10.1107/S0907444910007493.
[46] P.D. Adams, P.V. Afonine, G. Bunkóczi, V.B. Chen, I.W. Davis, N. Echols, J.J. Headd, L.W. Hung, G.J. Kapral, R.W. Grosse-Kunstleve, A.J. McCoy, N.W. Moriarty, R. Oeffner, R. J. Read, D.C. Richardson, J.S. Richardson, T.C. Terwilliger, P.H. Zwart, PHENIX: a comprehensive Python-based system for macromolecular structure solution, Acta Crystallogr. Sect. D Biol. Crystallogr. 66 (2010) 213–221, https://doi.org/10.1107/S0907444909052925.
[47] E.F. Pettersen, T.D. Goddard, C.C. Huang, G.S. Couch, D.M. Greenblatt, E.C. Meng, T.E. Ferrin, UCSF Chimera—a visualization system for exploratory research and analysis, J. Comput. Chem. 25 (2004) 1605–1612, https://doi.org/10.1002/jcc.20084.